JOURNAL OF GEOPHYSICAL RESEARCH, VOL. ???, XXXX, DOI:10.1029/,

Wavelength dependence of solar flare irradiation and its influence on the thermosphere

Yanshi Huang,[1] Arthur D. Richmond,[2] Yue Deng,[1] L. Qian,[2] S. Solomon,[2] P. Chamberlin,[3]

Y. Huang, Department of Physics, University of Texas, Arlington, TX 76019, USA. (yanshi.huang@mavs.uta.edu)

A. D. Richmond, High Altitude Observatory, National Center for Atmospheric Research, Boulder, CO 80307, USA.

Y. Deng, Department of Physics, University of Texas, Arlington, TX 76019, USA.

L. Qian, High Altitude Observatory, National Center for Atmospheric Research, Boulder, CO 80307, USA.

S. Solomon, High Altitude Observatory, National Center for Atmospheric Research, Boulder, CO 80307, USA.

P. Chamberlin, Solar Physics Laboratory, NASA Goddard Space Flight Center, Greenbelt, MD 20771, USA.

[1]Department of Physics, University of Texas

Abstract.

The wavelength dependence of solar flare enhancement is one of the important factors determining how the Thermosphere-Ionosphere (T-I) system response to flares. To investigate the wavelength dependence of solar flare, the Flare Irradiance Spectral Model (FISM) has been run for 34 X-class flares. The results show that the percentage increases of solar irradiance at flare peak comparing to pre-flare condition have a clear wavelength dependence. In the wavelength range between 0 - 195 nm, it can vary from 1% to 10000%. The solar irradiance enhancement is largest (1000%) in the XUV range (0 - 25 nm), and is about 100% in EUV range (25 - 120 nm). The influence of different wavebands on the T-I system during the October 28th, 2003 flare (X17.2-class) has also been examined using the latest version of National Center for Atmospheric Research (NCAR) Thermosphere-Ionosphere-Electrodynamics General Circulation Model (TIE-GCM). While

at Arlington, Texas, U.S.A.

[2]High Altitude Observatory, National Center for Atmospheric Research, Boulder, Colorado, U.S.A.

[3]Solar Physics Laboratory, NASA Goddard Space Flight Center, Greenbelt, Maryland, U.S.A.

the globally integrated solar energy deposition is largest in the 0 - 14 nm waveband, the impact of solar irradiance enhancement on the thermosphere at 400 km is largest for 25 - 105 nm waveband. The effect of 122 - 195 nm is small in magnitude, but it decays slowly.

1. Introduction

Solar flare is a sudden, intense release of magnetic energy in the atmosphere of the Sun, which produces rapid increase in electromagnetic radiation from gamma rays to radio wavelengths. One can classify a flare as a C, M, or X flare according to the maximum flux of soft X-ray flux in the 0.1 - 0.8 nm range of the spectrum measured near the Earth [*Garcia*, 2000]. While C-class flares are a common occurrence during years near solar maximum, the frequency of X-class flares is always low. The solar UV photons are a heating source to the neutral and ionized constituents of the thermosphere-ionosphere (T-I) system. The extra ionization in the ionosphere caused by flares increases electron density, which influences the absorption and refraction of radio waves propagating through the ionosphere from one station to another. Also, flares are often associated with coronal mass ejection (CME), which may cause significant geomagnetic storms [*Tandberg-Hanssen and Emslie*, 1988].

Previously, studies of the thermospheric and ionospheric responses to solar flares have been conducted [*Tsurutani et al.*, 2005; *Sutton et al.*, 2006; *Zhang et al.*, 2011]. The impacts of flares to T-I system varies because flares may have different magnitudes, locations on the solar disk, rise rates and decay rates. The enhancement of the extreme ultraviolet (EUV) spectral irradiance depends on the location of a flare, while flare enhancement of soft X-ray (XUV) depends weakly on the location [*Qian et al.*, 2010]. There is also a large spectral difference between flares in magnitude [*Thomson et al.*, 2004]. We expect that the impact of solar flare to the upper atmosphere depends on the spectral components with different wavelength, which not only have different irradiance, but also ionize different parts of the upper atmosphere. The

XUV dominates ionization in the lower thermosphere ($< 150km$), while EUV dominates in the upper thermosphere [*Qian et al.*, 2011].

The purpose of this paper is to investigate how different wavebands of solar flare impact thermosphere and ionosphere. We use the National Center for Atmospheric Research (NCAR) Thermosphere-Ionosphere-Electrodynamics General Circulation Model (TIE-GCM) [*Roble and Ridley*, 1994] to simulate the thermospheric and ionospheric responses to idealized flares. Flare spectra estimated by the Flare Irradiance Spectral Model (FISM) [*Chamberline et al.*, 2007, 2008] are used as solar input to TIE-GCM. The solar flare spectrum is divided into 6 different wavebands: 0 - 14 nm, 14 - 25 nm, 25 - 105 nm, 105 - 120 nm, 121.56 nm ($Lyman - \alpha$) and 122 - 195 nm. Due to large variations during flares for different wavelengths and lack of measurements from SEE, the uncertainty of FISM flare component has wavelength dependence and varies from 10% to above 100%. However, compared to models with only daily components, FISM improves the estimation of solar flares significantly.

2. Model Description

2.1. FISM Solar Flare Model

Flare Irradiance Spectral Model (FISM) is an empirical model of the solar irradiance spectrum from 0.1 to 195 nm at 1nm resolution and on 1-minute time cadence. The high temporal resolution of FISM makes it possible to study the variations due to solar flares. This model is based on the data provided by the Solar Extreme ultraviolet Experiment (SEE) on the Thermosphere Ionosphere Mesosphere Energetic and Dynamics (TIMED) satellite and the Solar Stellar Irradiance Comparison Experiment (SOLSTICE) on the Upper Atmosphere Research Satellite (UARS). The flare component of FISM including both the impulsive and gradual phase variations is based on a reference set of 39 large flares from 2002 to 2005 measured by the TIMED SEE [*Chamberline et al.*, 2008].

2.2. NCAR TIE-GCM

The latest version (v1.94) of the National Center for Atmospheric Research (NCAR) TIE-GCM is employed. TIE-GCM is a first-principle, three-dimensional, non-linear representation of the coupled thermosphere and ionosphere system. It solves the momentum, energy and continuity equations for neutral and ion species in pressure coordinates [*Roble et al.*, 1988], with a self-consistent calculation of ionospheric wind dynamo effects [*Richmond et al.*, 1992]. The external forcing of TIE-GCM are mainly the solar irradiance, magnetospheric energy, and tidal perturbations at the lower boundary of the model. Magnetospheric energy inputs include auroral particle precipitation and high-latitude ion convection. The Heelis potential model [*Heelis et al.*, 1982] is used to specify the high-latitude electric field in this study. The TIE-GCM is run with $5° \times 5° \times$ half scale height resolution (longitude $\times$ latitude $\times$ altitude).

Another NCAR upper atmospheric model, Thermosphere-Ionosphere-Mesosphere-Electrodynamics General Circulation Model (TIME-GCM) [*Roble and Ridley*, 1994] covers the altitudinal range from 30 km to 600 km, including mesosphere. Compared to TIE-GCM, TIME-GCM includes absorption in UV wavelengths such as O_2 absorption in Shumann-Runge continuum and Shumann-Runge bands, and O_3 dissociation from the Herbzberg, Hartley, Huggins, and Chapius bands [*Qian et al.*, 2011]. However, TIE-GCM and TIME-GCM use the same solar energy deposition scheme for the XUV and EUV, and also photoionization is calculated for the altitude above 97 km for both TIE-GCM and TIME-GCM. Therefore, both could be used for flare study.

3. Results

3.1. FISM data for X-class flares

Figure 1 depicts the FISM outputs for a X17.2 flare on October 28th, 2003 (day of year 301). The top panel shows the time variation of total solar flux integrated for 0 - 195 nm wavelength, which started to increase at 11:00 UT and reached maximum flux 100 mW/m^2 at around 11:07 UT. The wavelength dependences of solar flux before flare and at flare peak are shown in the middle panel. The pre-flare dependence is in black which is also denoted by the triangle in the top panel, while the red line is for the time at flare peak which is denoted by diamond in the top panel. The flux enhancement varies for different wavelengths, which is also illustrated in the bottom panel, the percentage increase of solar flux comparing the flare peak to the pre-flare condition has wavelength dependence. In the wavelength range between 0 - 195 nm, the percentage increase can vary from several percents up to 10000%. The solar irradiance increased largest in the XUV range, about 1000% on average, and increased about 100% in EUV range on average.

To have a better understanding of the wavelength dependence of percentage increase of X-class flares, we examine the spectra of 34 X-class flares observed between year 1989 and 2012 using FISM. As depicted in Figure 2, the percentage increase can vary from 0.1% up to 10000% depending on the wavelength in 0 - 195 nm range. There is not very large enhancement in 15 - 25 nm wavelength range, which contains many strong solar emission lines, such as the Fe IX. When a flare happens these emissions don't increase very much, and sometimes even decrease. This is because most of these emissions are formed in the solar corona at the approximate temperatures of the corona around 1 to 2 million degrees (Kelvin). When there is a significant heating that heats the source ions to much higher temperatures, Fe IX quickly becomes Fe XX, for example.

Therefore, the source ion population is depleted [*Woods et al.*, 2011]. The low enhancement in 115 - 129 nm range is rather instrumental. In the TIMED/SEE instrument, which FISM is based on, an Aluminum filter had to be put in place to block 99% of the $Lyman - \alpha$ emission line at 121.56 nm so that it will not saturate the detector [*Eparvier et al.*, 2001]. However, it does not allow the 'wings' on each side to be measured significantly. Therefore, they all behave very close to the $Lyman - \alpha$ emission in the model. It was also found that there is an approximately linear relation between solar irradiance in wavelength 0.1 - 0.8 nm and irradiance in 0 - 14 nm, which are all coronal emission [*Chamberline et al.*, 2008].

The solar spectra from FISM is used as the solar input for TIE-GCM. Since the purpose of our study in this paper is to investigate the thermospheric response to flares in different wavelengths, the penetration depths of solar irradiance with different wavelengths through the atmosphere should also be a criteria to divide the spectra into different wavebands. The local absorption rate depends on the product of absorption cross-section and the total abundance of the absorbing species along the path, which is known as the optical depth. The maximum absorption occurs at the altitude where the optical depth is unit. According to the wavelength dependence of altitude for unit optical depth shown in Figure 1 in *DeLand and Cebula* [2012] (adapted from [*Meier*, 1991]), we divide the whole irradiance spectra from 0 - 195 nm into 6 different wavebands: 0 - 14 nm, 14 - 25 nm, 25 - 105 nm, 105 - 120 nm, 121.56 nm, 122 - 195 nm.

3.2. Response of high-altitude thermosphere to flare at different wavelengths

As discussed above, in order to investigate the influence of solar flare at different wavelengths, we divide the irradiance spectra of FISM (0 - 195 nm) into six different wavebands: 0-14 nm and 14-25 nm wavebands for XUV irradiance, 25-105 nm and 105-120 nm for EUV irradiance, Lyman-alpha line (121.56 nm) and 122-195 nm waveband for far ultraviolet (FUV) irradiance. On October 28th, 2003 (Day of year, 301), there was a X17.2-class solar flare, which was one of the most severe flares in the last solar cycle. For each waveband, for example, 0 - 14 nm wavelengths, we run 2 cases using TIE-GCM. For case 1, we run TIE-GCM using constant solar input at pre-flare condition for DOY 301, and for case 2, using time varying solar input only within 0 - 14 nm wavelength. The difference between these two runs represents the influence of solar irradiance within 0 - 14 nm waveband to the thermosphere. The influences of solar irradiance within other wavebands are also calculated in this way. To minimize geomagnetic influences, all the simulations are under the geomagnetic quiet condition ($Kp = 1$). In this study, the results are analyzed in terms of values integrated or averaged over the globe.

Figure 3 shows the temporal variations of solar irradiance flux in 0 - 14 nm, 25 - 105 nm and 122 - 195 nm wavebands and their influences on the thermosphere. We only show the wavebands of FISM spectrum which have non-negligible thermospheric effect. The solar flux variations for different wavebands calculated from FISM are depicted in the first panel, which illustrates that the solar flux in 0 - 14 nm waveband was quite small before flare compared to that in 122 - 195 nm waveband, but it increased most by about 20 mW/m^2. The second panel shows the enhancements of globally integrated solar energy deposition in the upper atmosphere during the flare. The peak of solar energy deposition for 0 - 14 nm is the largest and almost three times larger than the peak for 25 - 105 nm, which is also shown in table 1. However, the time integration of global solar energy (TIGSE) for 25 - 105 nm waveband is only half of the TIGSE for 0 - 14 nm and even larger than the one for 122 - 195 nm waveband. The third panel depicts the Joule heating enhancement that shows quite different responses in time and magnitude for different wavebands. There is a rather rapid and large enhancement of Joule heating responding to the solar flare irradiance for 0 - 14 nm waveband, however, for 122 - 195 nm, the peak of Joule heating enhancement is negligible and has a obvious delay to the flare peak. The response for 25 - 105 nm is somewhat combination of the ones for 0 - 14 nm and 122 - 195 nm wavebands. The total timely integration of global solar energy increased by 6.79e10 J for the solar flare on October 28th, 2003, while the timely integration of global joule heating increased comparably little by 1.86e09 J. The fourth and bottom panels depict the thermospheric temperature and density perturbations at 400 km. The altitude 400 km was chosen because this is the altitude range where low-Earth satellites fly. As also illustrated in table 1, although the largest energy deposition comes from solar irradiance in 0 - 14 nm wavelength, most of the thermospheric perturbations at 400 km are due to 25 - 105 nm waveband while the impact of 122 - 195 nm is negligible. The high-altitude temperature and density perturbations divided by the solar energy deposition peak or the TIGSE is an order larger for 25 - 105 nm waveband than those for the other two wavebands. Therefore, the solar irradiance in 25 - 105 nm of EUV influences the high-altitude thermosphere most effectively. The high-altitude temperature and neutral density response $3 \sim 5$ hours later than the flare peak, as a result of the different energy deposition heights and amounts for irradiance with different wavelengths. As discussed in *Huang et al.* [2012], the characteristic response timescale of the upper-thermosphere depends on the height of heat deposition, as shown in Figure 4. The temperature response at 400 km to the high-altitude heating is much stronger and faster than the response to low-altitude heating.

3.3. Response of T-I system to flare at different wavelengths at flare peak

Figure 4 depicts the altitudinal distributions of perturbations due to solar irradiance in different wavebands at the flare peak. Most of the solar energy is deposited below 150 km by the 0 - 14 nm and 122 - 195 nm wavebands, while the energy deposition in 25 - 105 nm dominates above $\sim$ 160 km. This results in the largest perturbations of electron density and Pedersen conductivity due to 0 - 14 nm waveband in E region and due to 25 - 105 nm in F region. Enhancement of the 122-195nm waveband impacts the thermosphere through dissociation, which results in little effect on the electron density and Pedersen conductivity variation. The temperature perturbation below $\sim$150 km is also largest due to energy deposition in 0 - 14 nm and 122 - 195 nm wavebands, while for the upper thermosphere it is largest due to deposition in 25 - 105 nm. Therefore, the solar radiation in 25 - 105 nm is important for high altitude ionization and heating at flare peak.

3.4. Temporal variation of thermospheric enhancements due to solar irradiance at different wavelengths

The enhancements were calculated through taking the difference between the flare and non-flare runs for each waveband. Figure 5, 6, 7 and 8 show the temporal variations of the altitudinal distribution of solar energy deposition percentage increase, Pedersen conductivity percentage increase, temperature increase and neutral density percentage increase due to solar irradiance in different wavelengths. The line plots represent the temporal variations at 400 km altitude. As shown in Figure 5, the total solar energy deposited into the upper atmosphere increases up to 140% due to the solar irradiance enhancement within 0 - 195 nm, initially deposited under 150 km but lasts longer in the higher altitude. The Pedersen conductivity enhancement can reach up to 300% in low altitudes. The absorption rate at an arbitrary altitude is proportional to the multiplication of neutral density and photon flux. Changes in the upper atmosphere following a flare might not simply due to the thermal inertia of the atmosphere, but might partly due to the fact that the altered density structure of the atmosphere absorbs non-flare irradiance differently from before the flare. For example, it is possible that the GSE enhancement at high altitudes after the flare is not due to the residual flare irradiance, but rather to the fact that the neutral density has increased, so that more non-flare irradiance is absorbed at a given altitude. The maximum of temperature enhancement is 45 K and the maximum of density enhancement is about 17%, which are both found in high altitudes and have $3 \sim 4$ hour time delay to the flare peak. As discussed previously, the thermospheric response at 400 km to the high-altitude heating is much stronger and faster than the response to low-altitude heating [*Huang et al.*, 2012].

We divide the whole spectrum from 0 - 195 nm into different wavebands and investigate the impact of each waveband on the T-I system. As illustrated in the comparison of Figure 6, 7 and 8, the temporal and altitudinal response of T-I system to solar flare irradiance varies significantly with irradiance wavebands. Although the maximum percentage increase of energy deposition is about 100%, the solar energy enhancement peaks at lower altitude below 150 km for 0 - 14nm, while the solar energy in 25 - 105 nm waveband deposited at higher altitude and increases up to 70%. The disturbances in T-I system, for example, globally averaged Pedersen conductivity, temperature and neutral density show that most of the high-altitude perturbations are due to 25 - 105 nm (part of EUV) waveband. Also, the energy deposition enhancement in 122 - 195 nm waveband is below 150 km and impacts the thermosphere through dissociation, therefore, it has little effect on Pedersen conductivity, temperature and neutral density. However, the temperature and neutral density perturbations due to solar irradiance in this waveband do not decay as fast as those due to irradiance in 0 - 14 nm and 25 - 105 nm.

Figure 9 illustrates the nearly linear response of T-I system at 400 km to different wavebands of solar irradiance. The black lines represent the globally averaged perturbations of solar energy deposition, neutral density , temperature and electron density at 400 km due to the whole flare spectrum from 0 to 195 nm, while the red lines represent the summations of perturbations at 400 km due to 6 separated bands. The high-altitude response to the flare spectra in 0 - 195 nm is almost a linear combination of those to separated wavebands, which suggests a possibility to predict the variations of temperature, neutral and electron density at satellites orbits responding to the future flares according to the solar irradiance enhancement measured at different wavebands.

4. Conclusions

The response of T-I system to flare irradiance could be different in magnitude and duration due to the flares with different deposition heights, magnitudes of enhancement and durations for different wavebands. The wavelength dependence of solar flare enhancement is one of the important factors determining how the terrestrial atmosphere response to flares with different enhancement in wavelength. The FISM data show that for the 34 X-class solar flares between year 1989 and 2012, the solar irradiance comparing the flare peak to the pre-flare condition has wavelength dependence. In the wavelength range between 0 - 195 nm, the percentage increase can vary from 1% to 10000%. The solar irradiance increased largest in the XUV range (0 - 25 nm), about 1000% on average, and the one in EUV range (25 - 120 nm) increased about 100% on average.

In this paper, we investigate how the thermosphere and ionosphere respond to the different wavebands of solar irradiance for the X17.2-class solar flare on October 28th, 2003. The solar irradiance spectra of FISM (0 - 195 nm) is divides into six different wavebands: 0-14 nm and 14-25 nm wavebands for XUV range, 25-105 nm and 105-120 nm for EUV, $Lyman-\alpha$ line (121.56 nm) and 122-195 nm waveband for FUV. For each waveband, for example, 0 - 14 nm wavelengths, we run 2 cases using TIE-GCM, one case 1 with constant solar input at pre-flare condition, and the other case with time varying solar input only within 0 - 14 nm wavelength. The enhancements are calculated through taking the difference between the flare and pre-flare runs. The globally integrated solar energy deposition and the time integration of it was largest due to 0-14nm waveband compared to other wavebands. However, the time integration of Joule heating energy enhancement due to solar irradiance increases comparably for 0-14nm and 25-105nm wavebands. The impact of solar irradiance enhancement on the thermosphere at 400 km is largest for 25 - 105 nm waveband, which accounts for about 33 K in total 45 K temperature disturbance, and about 7.4% in total 11% neutral density disturbance. The effect of 122 - 195 nm irradiance is little in magnitude, since it impacts the thermosphere through dissociation. Therefore, the solar irradiation at 25 - 105 nm impacts high-altitude heating and ionization most effectively.

For the future work, we plan to investigate more X-class solar flare events with different magnitudes and durations to get a better understanding and conclusion of their influences at different wavelengths.

Acknowledgments. We acknowledge the LASP Interactive Solar Irradiance Data center for FISM data. This research was supported by the National Science Foundation through grant ATM0955629. Part of this work was conducted while Y.H. and Y.D. were visitors in the Advanced Study Program at the National Center for Atmospheric Research (NCAR). NCAR is sponsored by the National Science Foundation.

References

Barth, C. A., G. Lu, and R. G. Roble (2009), Joule heating and nitric oxide in the thermosphere, J. Geophys. Res., 114, A05301, doi:10.1029/2008JA013765.

Chamberlin, P. C., T. N. Woods, and F. G. Eparvier (2007), Flare Irradiance Spectral Model (FISM): Daily component algorithms and results, Space Weather, 5, S07005, doi:10.1029/2007SW000316.

Chamberlin, P. C., T. N. Woods, and F. G. Eparvier (2008), Flare Irradiance Spectral Model (FISM): Flare component algorithms and results, Space Weather, 6, S05001, doi:10.1029/2007SW000372.

DeLand, M. T. and Cebula, R. P.: Solar UV Variations During the Decline of Cycle 23, J. Atmos. SolTerr. Phys., 77, 225234, doi:10.1016/j.jastp.2012.01.007, 2012. 7041, 7056

Einar Tandberg-Hanssen and A. Gordon Emslie: The Physics of Solar Flares. Cambridge Astrophysics Series. Cambridge University Press, Cambridge-New York-New Rochelle-Melbourne-Sydney 1988.

Eparvier, F. G., T. N. Woods, G. J. Ucker, and D. L. Woodraska (2001), TIMED solar EUV experiment: preflight calibration results for the EUV grating spectrograph, SPIE Proc., 4498, 91100, doi:10.1117/12.450049.

Garcia,H.A. (2000), Thermal spatial analysis ofmedium and large solar flares: 1976 to 1996, Astrophys. J., 127, suppl., 189210, doi:10.1086/313312.

Heelis, R., J. Lowell, and R. Spiro (1982), A Model of the High?Latitude Ionospheric Convection Pattern, J. Geophys. Res., 87(A8), 6339-6345.

Huang, Y., A. D. Richmond, Y. Deng, and R. Roble (2012), Height distribution of Joule heating and its influence on 24 the thermosphere, J. Geophys. Res., 117, AXXXXX, doi:10.1029/2012JA017885.

Meier, R. R., 1991. Ultraviolet spectroscopy and remote sensing of the upper atmosphere. Space Sci. Rev. 58, 1-185.

Qian, L., A. G. Burns, P. C. Chamberlin, and S. C. Solomon (2010), Flare location on the solar disk: Modeling the thermosphere and ionosphere response, J. Geophys. Res., 115, A09311, doi:10.1029/2009JA015225.

Qian, L., A. G. Burns, P. C. Chamberlin, and S. C. Solomon (2011), Variability of thermosphere and ionosphere responses to solar flares, J. Geophys. Res., 116, A10309, doi:10.1029/2011JA016777.

Richmond, A. D., E. C. Ridley, and R. G. Roble (1992), A thermosphere/ ionosphere general circulation model with coupled electrodynamics, Geophys. Res. Lett., 19, 601604.

Roble, R. G., E. C. Ridley, A. D. Richmond, and R. E. Dickinson (1988), A coupled thermosphere/ionosphere general circulation model, Geophys. Res. Lett., 15, 13251328.

Roble, R. G., and E. C. Ridley (1994), A thermosphere-ionosphere-mesosphere electrodynamics general circulation model (TIME-GCM): Equinox solar cycle minimum simulations (30500 km), Geophys. Res. Lett., 21, 417420, doi:10.1029/93GL03391.

Sutton, E. K., J. M. Forbes, R. S. Nerem, and T. N.Woods (2006), Neutral density response to the solar flares of October and November, 2003, Geophys. Res. Lett., 33, L22101, doi:10.1029/2006GL027737.

Thomson, N. R., C. J. Rodger, and R. L. Dowden (2004), Ionosphere gives the size of greatest solar flare, Geophys. Res. Lett., 31, L06803, doi:10.1029/2003GL019345.

Tsurutani, B. T., et al. (2005), The October 28, 2003 extreme EUV solar flare and resultant extreme ionospheric effects: Comparison to other Halloween events and the Bastille Day event, Geophys. Res. Lett., 32, L03S09, doi:10.1029/2004GL021475.

Woods, T.N., Hock, R., Eparvier, F., Jones, A.R., Chamberlin, P.C., Klimchuk, J.A., Didkovsky, L., Judge, D., Mariska, J., Warren, H., Schrijver, C.J., Webb, D.F., Bailey, S., Tobiska, W.K.:

2011, New solar extreme-ultraviolet irradiance observations during flares. Astrophys. J. 739, 59. doi:10.1088/0004-637X/739/2/59.

Zhang, D. H., X. H. Mo, L. Cai, W. Zhang, M. Feng, Y. Q. Hao, and Z. Xiao (2011), Impact factor for the ionospheric total electron content response to solar flare irradiation, J. Geophys. Res., 116, A04311, doi:10.1029/2010JA016089.

Table 1. Heating efficiency of solar irradiance at different wavelengths to thermosphere at 400 km.

	$0-14$ nm	$25-105$ nm	$122-195$ nm
δSE peak (GW)	1216	379	548
TIGSE (J)	3.48e10	1.85e10	1.08e10
δTn peak (K)	8.4	32.8	1.2
$\delta\rho$peak	2.50%	7.39%	0.58%
δTn$/\delta$SE (K/GW)	0.0069	0.0865	0.0022
δTn/TIGSE (K/J)	2.41e-10	17.73e-10	1.09e-10
$\delta\rho/\delta$SE (%/GW)	0.0021	0.0200	0.0011
$\delta\rho/$TIGSE (%/J)	0.7e-10	4.0e-10	0.5e-10

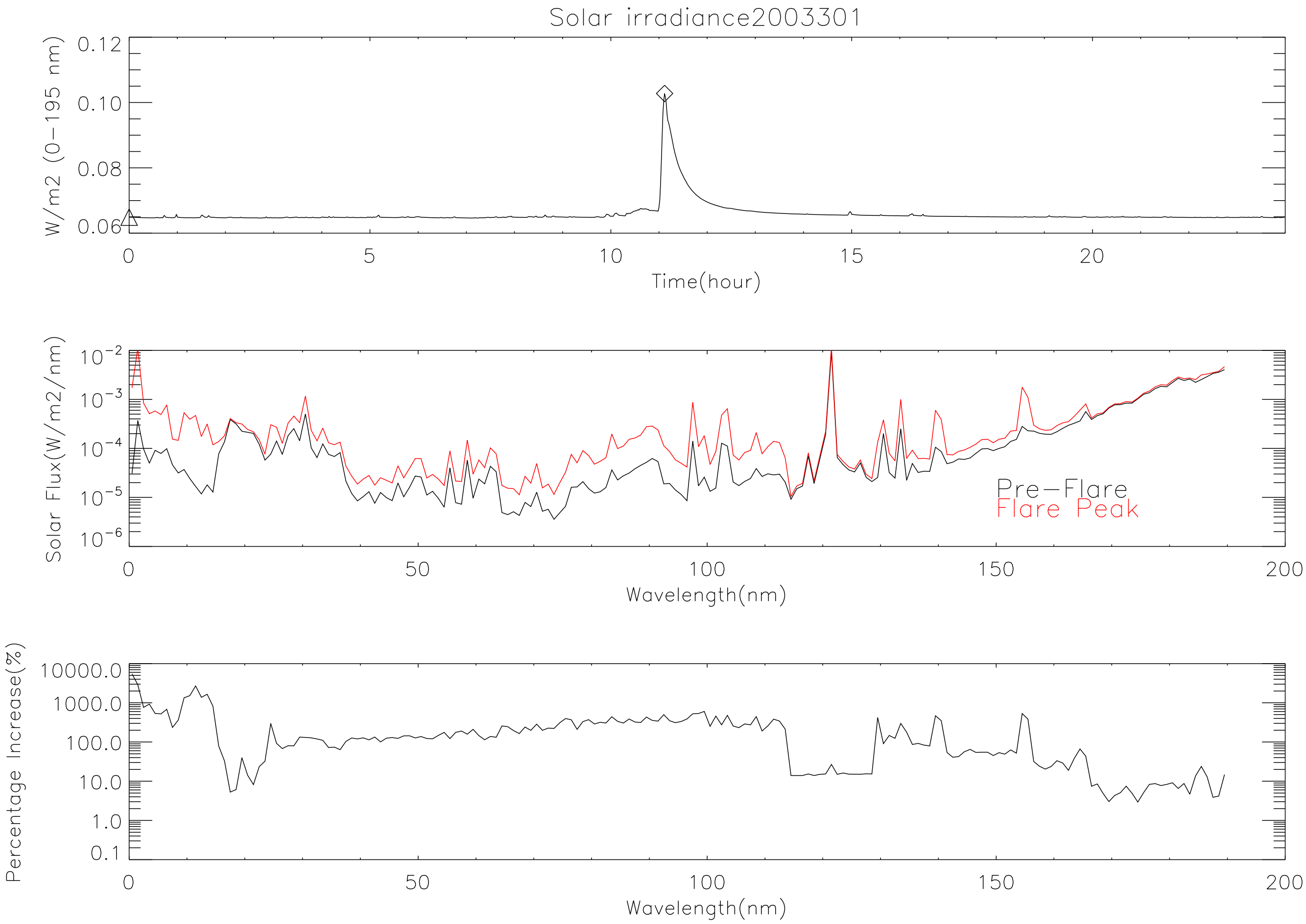

Figure 1. FISM solar irradiance results for X17.2 flare on October 28th, 2003 (day of year 301). Top: Time variation of total solar irradiance integrated over wavelength from 0 to 195 nm. The flare reached maximum flux 0.1 W/m^2 at around 11:07 UT. Middle: Solar spectra before flare at the moment denoted by triangle in top panel (black) and at flare peak denoted by diamond (red). Bottom: Percentage increase of solar irradiance comparing the peak and pre-flare conditions.

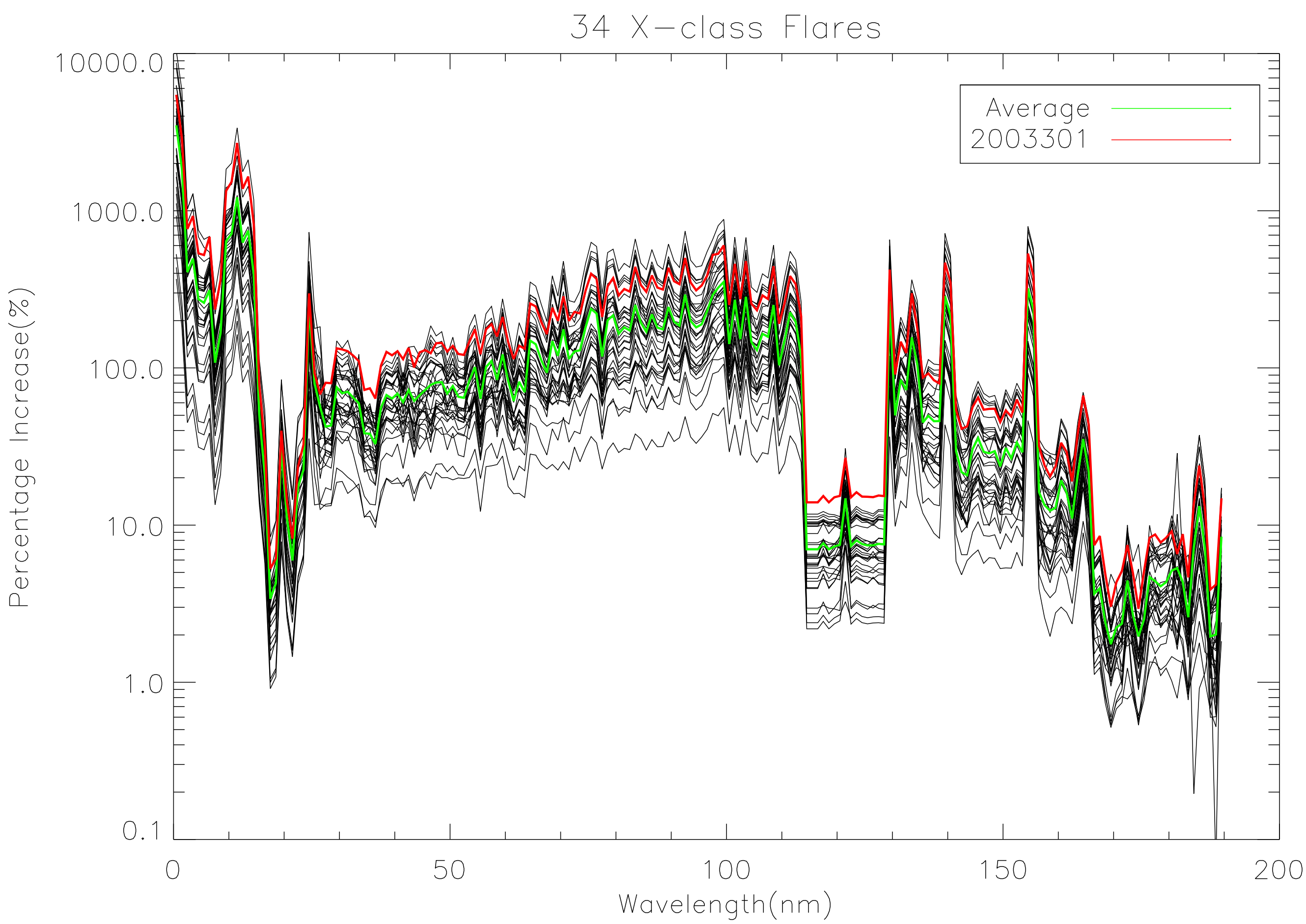

Figure 2. FISM solar irradiance results for percentage increases comparing the peak and pre-flare conditions for 34 X-class flares happened between year 1989 and 2012. The red line denotes the October 28th, 2003 flare event, and the green line is the average of 34 X-class flares. The low enhancement in 15 - 25 nm is a result of the depletion of source ion, while the low enhancement in 115 - 129 nm is rather instrumental.

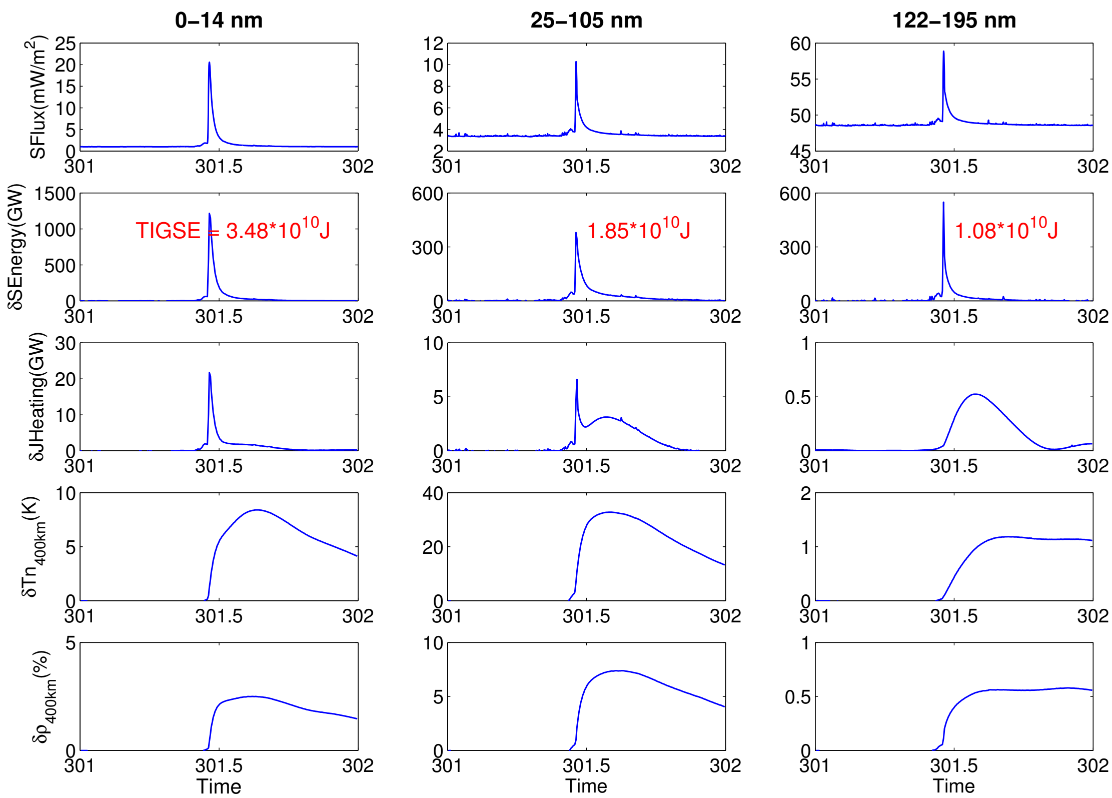

Figure 3. Time variations of different wavebands for DOY 301, first column for 0 - 14 nm, second column for 25 - 105 nm and third column for 122 - 195 nm. Top panel: Solar flux calculated from FISM. Second panel: Perturbation of global solar energy deposited into the upper atmosphere. The time integration of global solar energy (TIGSE) deposited are also labeled in red. Third panel: Perturbation of globally integrated Joule heating. Fourth panel: Globally averaged perturbation of temperature at 400 km. Bottom panel: Globally averaged perturbation of neutral density at 400 km.

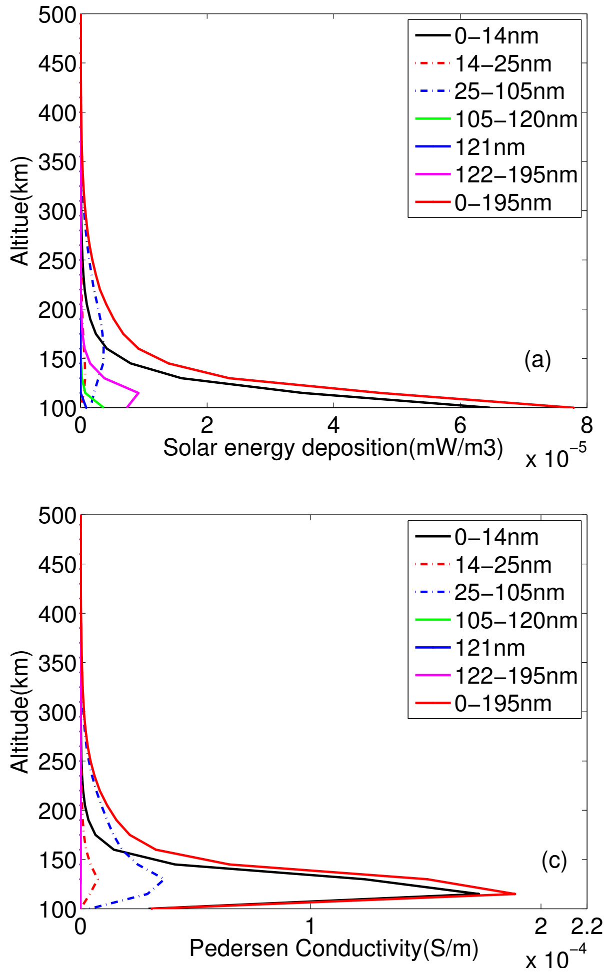

Figure 4. Altitudinal distribution of TIE-GCM simulation results at flare peak for solar irradiance in different wavelength ranges. (a) Globally averaged solar energy deposition. (b) Globally averaged electron density. (c) Globally averaged Pedersen conductivity. (d) Globally averaged temperature.

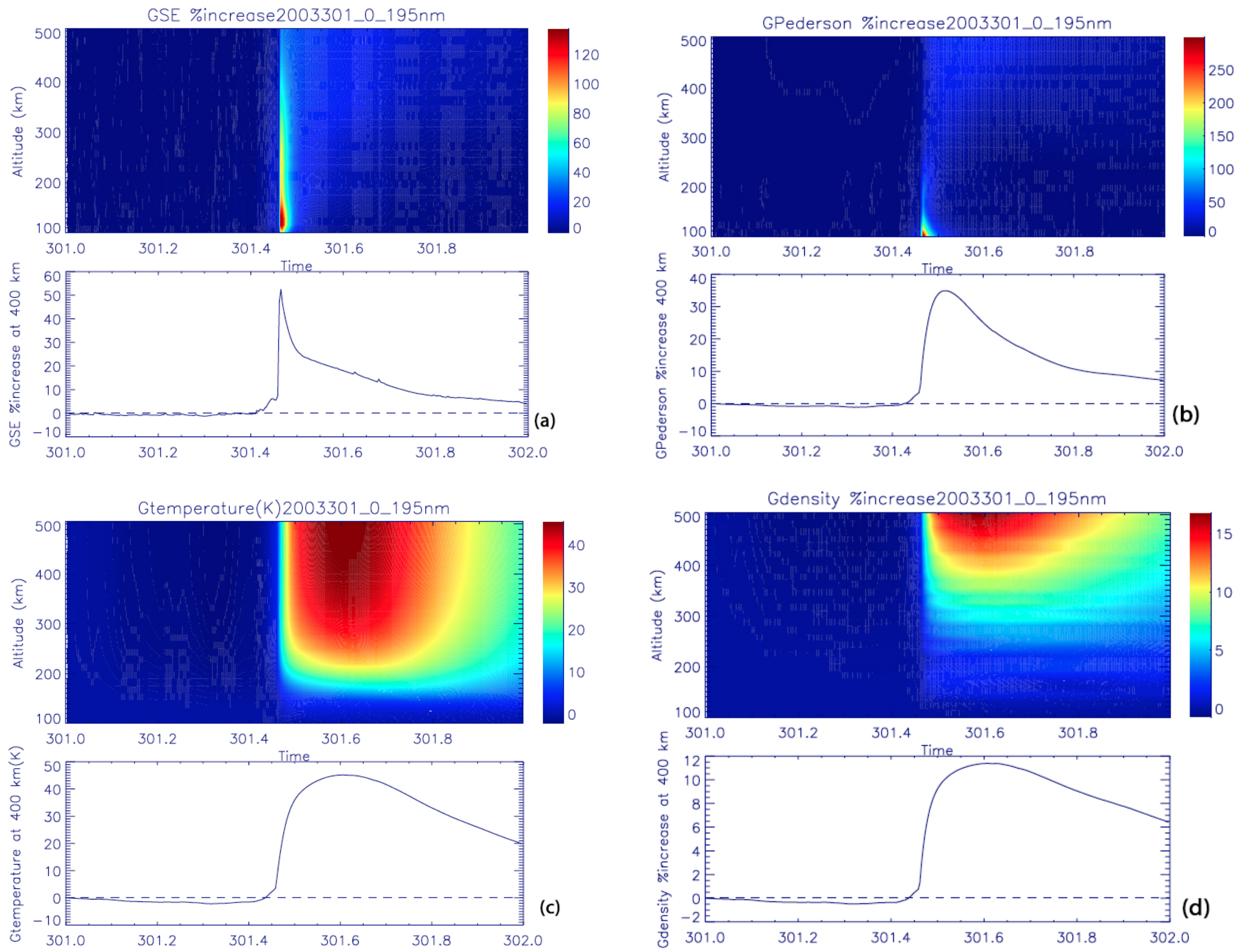

Figure 5. Temporal variations of the altitudinal distribution of TIE-GCM simulation results due to the solar irradiance enhancement in 0 - 195 nm wavelength range. (a) Globally averaged percentage increase of solar energy deposition. (b) Globally averaged percentage increase of Pedersen conductivity. (c) Globally averaged temperature enhancement. (d) Globally averaged percentage increase of neutral density. The line plots represent the temporal variations at 400 km altitude.

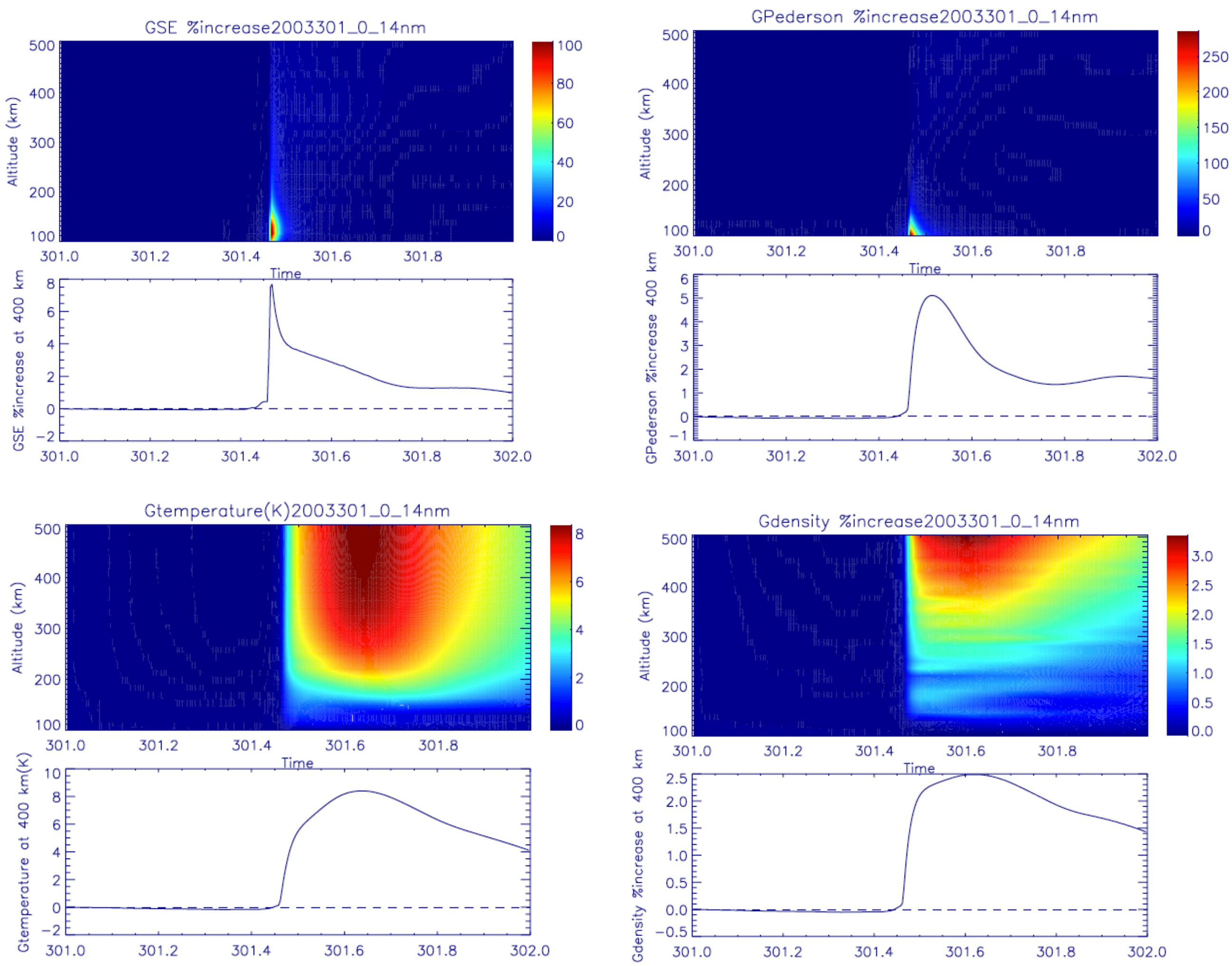

Figure 6. Same as Figure 5 but for the simulation results due to the solar irradiance enhancement in 0 - 14 nm wavelength range.

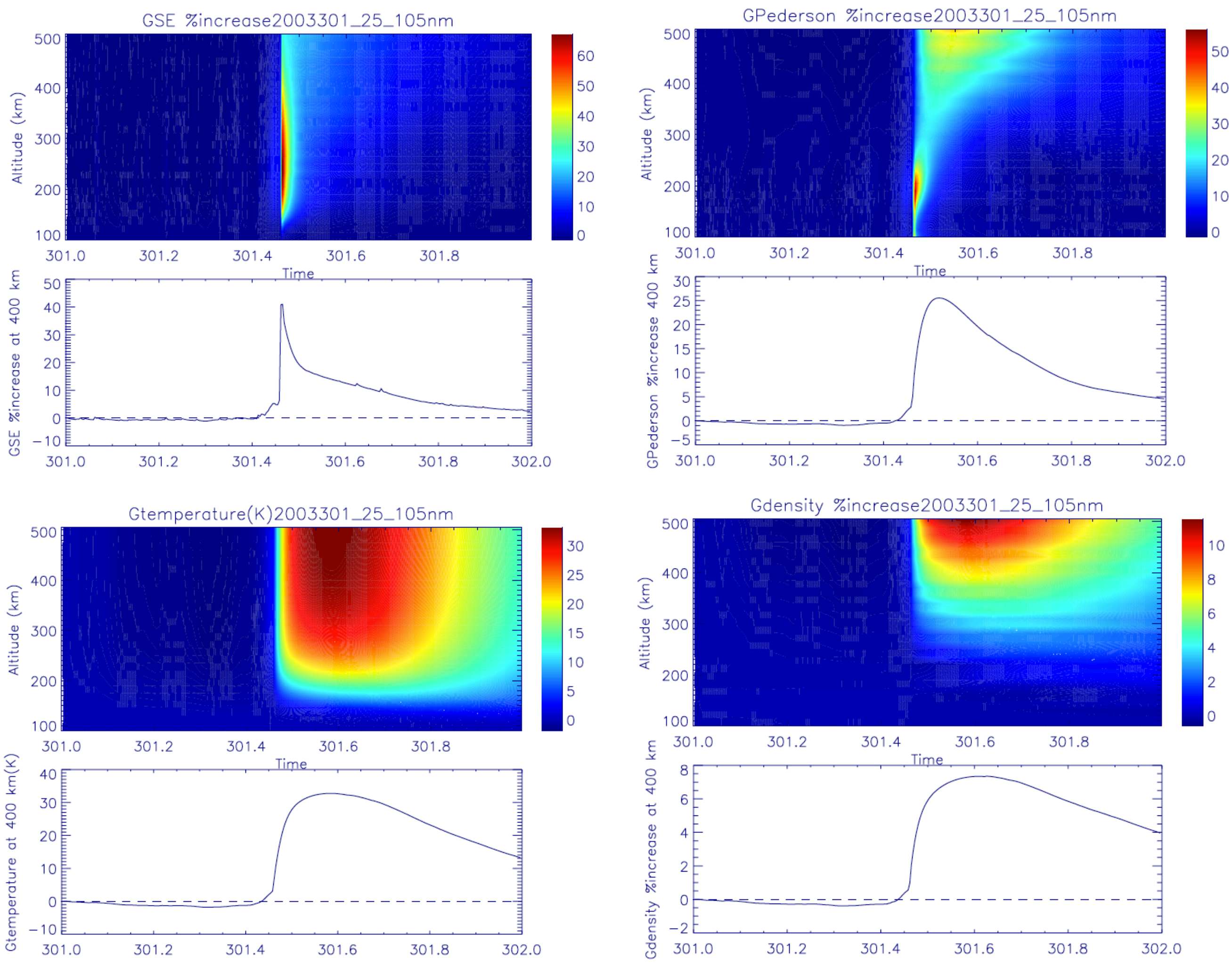

Figure 7. Same as Figure 5 but for the simulation results due to the solar irradiance enhancement in 25 - 105 nm wavelength range.

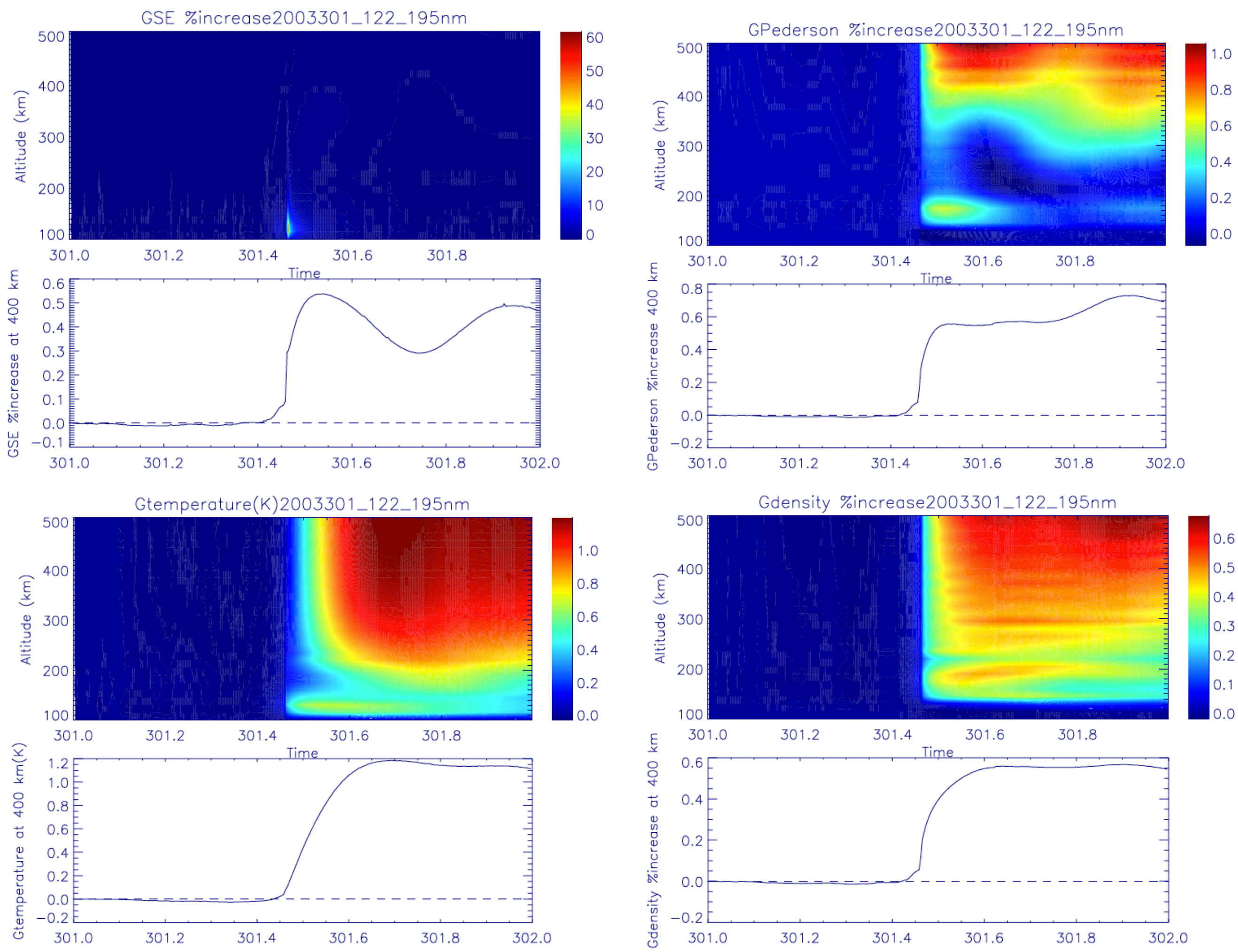

Figure 8. Same as Figure 5 but for the simulation results due to the solar irradiance enhancement in 122 - 195 nm wavelength range.

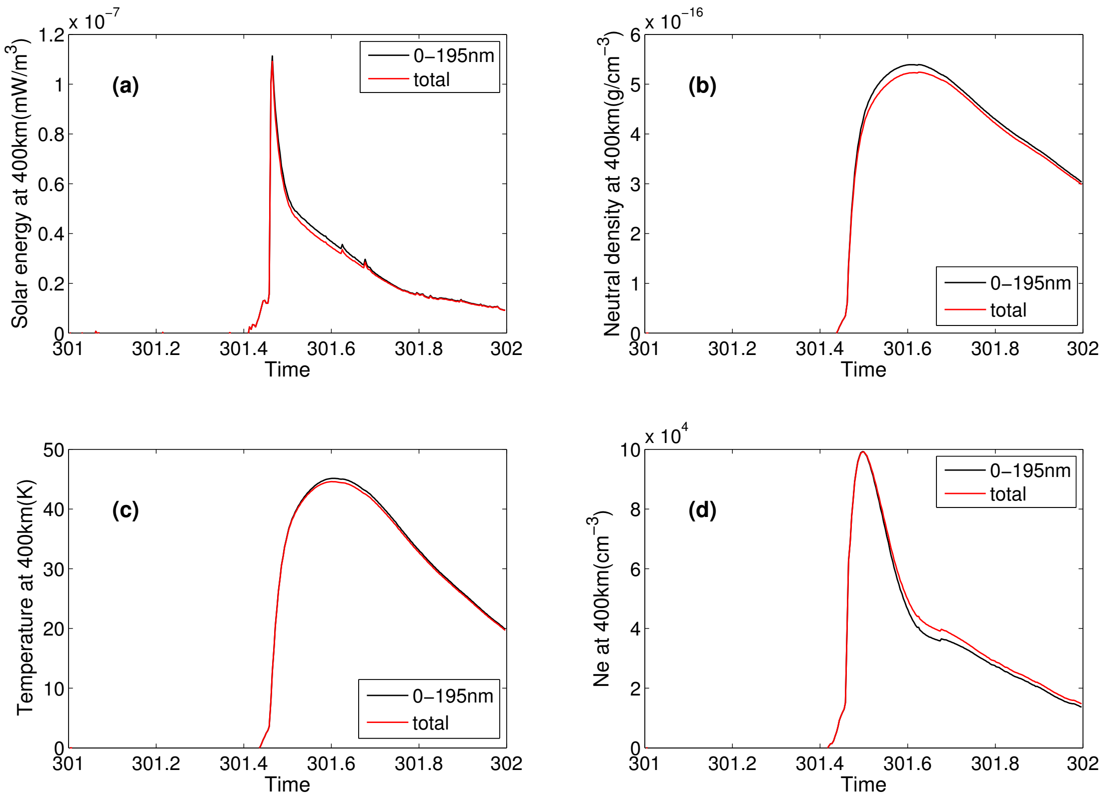

Figure 9. Comparison of TIE-GCM simulation results at 400 km. The black lines show the variations using FISM solar spectra in 0 - 195 nm as solar input, while the red lines represent the total sum of variations due to FISM spectra in separated wavebands. (a) Globally averaged solar energy deposited at 400 km. (b) Globally averaged neutral density at 400 km. (c) Globally averaged temperature at 400 km. (d) Globally averaged electron density at 400 km.